Sustainable nanocomposite thermoset of tannic acid-based epoxy and waste tea derived modified cellulose nanofibers

Highlights

The incorporation of carbon-based sustainable nanostructured cellulose nanofibers (CNFs) in a bio-epoxy (tannic acid epoxy, TAE) to achieve improved mechanical and thermal properties is the main focus of this chapter. CNFs were extracted from factory-generated waste tea fibers (WTFs) by mechanochemical treatments, which were further modified with amine-blocked isocyanate groups to introduce nitrogen-rich linkages to their surface. The functionalized CNFs (*f*-CNFs) were subsequently added as a nano-reinforcing agent to TAE with low loadings of 0.1, 0.2, and 0.3 weight percents. After scrutinizing the characteristics of the materials via different instrumental techniques, their mechanical, thermal, and chemical resistance properties were investigated. The potentiodynamic polarization studies demonstrated effective corrosion inhibition ability of the nanocomposites in corrosive environments. The accelerated biodegradation study further affirmed the environmental benevolence of the nanocomposites. The study revealed the potentiality of the sustainable nanocomposite as a mechanically tough and thermostable anticorrosion coating material.

Parts of this chapter is published in

Borah, N. and Karak, N. Cellulose Nanofibers modified with pendant amine groups as potential reinforcement in bioepoxy for a mechanically tough biodegradable anticorrosive nanocomposite coating. *Cellulose*, 2023, (***Under review, revised***).

4.1 Introduction

Biomass-derived cellulose nanofibers (CNFs) are quintessential high-performance nanostructured materials that have garnered appreciable attention in the present era because of their fascinating structural attributes [1]. These nanostructures comprise repeating β-(1,4)-D-glucose units arranged to form polymer chains with both amorphous and crystalline regions, which further assemble to form nanofibrils [2]. The fascinating attributes of CNFs, such as a high surface area with web-like network structures, low density, low coefficient of thermal expansion, and high mechanical strength, make them efficient reinforcing agents for polymers (such as epoxy) to fabricate nanocomposites [1]. CNFs are prevalently isolated from plants including hemp, bamboo, jute, banana, pineapple leaves, sisal, etc., and have dimensions varying from 5 to 200 nm in diameter and nearly 1 μm in length [2]. Manifold processing techniques such as high-pressure homogenization, ball milling, ultrasonication, chemical treatments, cryo-crushing, enzymatic treatments, etc. are employed for the isolation of CNFs from plant sources [3]. For instance, Ravindran et al. extracted CNFs with a diameter of 10-20 nm from pineapple leaves by using different chemical treatments [4]. Nagarajan et al. adopted a facile method by combining ball milling and chemical treatments for obtaining CNFs of diameter 55-64 nm from the peduncles of the *Cocos nucifera var-Aurantiaca* plant [3]. Waste tea fibers (WTFs) generated by tea factories are raw materials rich in cellulosic fibers but have rarely been explored in the realms of nanoscience. In the present investigation, WTFs have been employed for the extraction of CNFs using a facile method comprised of sequential chemical treatments and cryo-crushing.

As discussed in **Chapter One**, biobased epoxies are important polymeric materials, but because of some inherent discrepancies, they fail to effortlessly compete with petroleum-based commercial competitors (such as diglycidyl ether epoxy of bisphenol A, DGEBA) in terms of strength, thermal stability, etc. [5]. In this venture, using CNF as a reinforcing agent in such bio-epoxies can offer the foreseen performances. However, concerning their dispersion in a polymer matrix, the high hydrophilicity of CNFs instigates complications in homogenization with the hydrophobic matrix since the two phases have opposite polarities [6]. Additionally, CNF-reinforced epoxy nanocomposites are colossally utilized in different realms, but instances of the employment of CNF-based nanocomposites as barrier coatings for the protection of metallic surfaces are very limited [6]. Such under-exploration of CNFs as protective barriers in the field of anticorrosive

coatings could be primarily due to their hydrophilicity, which can be altered by designing state-of-the-art surface functionalization techniques. A plethora of methods are available that exemplify the modification or functionalization of CNF-surfaces with esters [7], ethers, amines [6], isocyanate [8], silanes [9], and suchlike, that not only improved the dispersion of CNFs in the polymer phase but also enhanced their performances. For example, Zhao et al. in 2017 functionalized CNFs with polyethyleneimine, which, upon incorporation into an epoxy matrix, elevated the tensile strength up to 88.1% compared to the pristine epoxy [6]. Bifunctional isocyanates and amines are good examples of such modifiers that have been individually employed on CNFs [8, 10]. However, no such attempt has been made till now to functionalize CNFs using amine-blocked isocyanates to produce urea-urethane linkages with an aim to attain better dispersion in bio-based epoxy matrices and to study their consequences on the overall performance of the epoxy, including the anticorrosion activity.

The present study is a proof of concept that illustrates a novel, and facile method for introducing pronounced enhancements in the mechanical properties of bio-epoxy resin using bio-derived CNFs enriched with urea-urethane linkage as reinforcing agents. The CNFs extracted from WTFs via chemical treatments assisted by cryo-crushing were further functionalized using toluene diisocyanate (TDI) and ethylene diamine (EDA) to introduce pendant amine groups on the surfaces of the CNFs. Subsequently, the integration of these modified CNFs with a tannic acid derived bio-based epoxy, TAE, resulted in mechanically tough, thermostable, and biodegradable epoxy nanocomposites. Furthermore, the performance of these nanocomposites as anticorrosive coatings was studied primarily via potentiodynamic polarization (PDP) studies to judge their practical applicability in the coating industries.

4.2 Experimental

4.2.1 Materials

2,4/2,6-TDI is an organic reactive compound with the chemical formula $CH_3C_6H_3(NCO)_2$ and the name 2,4/2,6-diisocyanato-1-methyl-benzene, according to the International Union of Pure and Applied Chemistry (IUPAC) nomenclature. It is a colorless liquid that has a molecular weight (m.w.) of 174.2 g/mol, a density of 1.22 g/cm^3, and a boiling point (b.p.) of 251 ℃. TDI is used as a chemical intermediate in the synthesis of polyurethane products, including foams, resins, etc. In the present investigation, 2,4/2,6-TDI is used for

the functionalization of CNFs and was procured from Merck, India, with a 98% purity index.

EDA or ethane-1,2-diamine is a colorless liquid with an ammonia-like odor. It has a m.w. of 60.06 g/mol, a density of 0.898 g/cm^3, and a b.p. of 116 ℃. It is an aliphatic diamine with the chemical formula $C_2H_8N_2$ and is basic in nature. Industrial production of EDA involves the reaction of 1,2-dichloroethane with ammonia under pressure at 180 ℃ in an aqueous medium. It is enormously used as ligands or in producing other chelating agents, while in polymer chemistry it is known for its crosslinker role. In this study, EDA was used for the functionalization of CNFs and obtained from Merck, India.

Hydrogen peroxide (H_2O_2) is a common oxidizing and bleaching agent. In its pure form, it is a pale blue liquid with a slightly lower viscosity than water. It has a m.w. of 34.01 g/mol, a density of 1.11 g/cm^3, and a b.p. of 150 ℃ at ambient conditions. H_2O_2 has a high solubility in water, ethanol, and acetone; the commercial form is available as a 3-5% (for household use) up to 35% aqueous solution. In this study, it is used for the bleaching of CNFs to remove coloring agents including lignin, and was obtained as a 30% aqueous solution for Merck, India.

Acetic acid, with the IUPAC name ethanoic acid, is the second simplest carboxylic acid, with the chemical formula CH_3COOH. It is a transparent, colorless liquid with a pungent smell and a sharp, sour taste. It has a m.w. of 60.05 g/mol, with a density of 1.05 g/cm^3, and a b.p. of 118 ℃. The acid strength of acetic acid is low, with a pKa value of 4.76. Acetic acid is obtained from Merck in India and was used for the extraction of CNFs from WTFs.

All other chemicals, such as tannic acid (TA), epichlorohydrin, and other auxiliary chemicals used in the production of TAE, WTFs, poly(amido amine), etc. are obtained from the same sources, with the same specifications as explained in **Chapter Two (Section 2.2.1)** and **Chapter Three (Section 3.2.1)**.

4.2.2. Instrumentation

The instruments used in the characterization and property evaluation of the CNFs, modified CNFs, and nanocomposites (such as FTIR, ATR-FTIR, TGA, DSC, SEM, UTM, impact, scratch hardness, etc.) are the same as explained in **Chapter Two,** in **Section 2.2.2** with similar processing and test conditions. The diffraction patterns of the CNFs, modified CNFs, and nanocomposites were recorded in a Bruker XS X-ray diffractometer (D8

FOCUS, Germany) using a copper Kα beam of wavelength 1.54 Å operating in the reflection mode. The crystallinity index (CrI) was calculated according to the Segal equation (**Equation 4.1**), as shown below [11].

$$CrI\ (\%) = [(I_{200} - I_{am})/I_{am}] \times 100 \qquad \textbf{Equation 4.1}$$

where I_{200} is the intensity of the peak corresponding to the 200 planes and I_{am} is the intensity of the amorphous region [9]. To study the size and morphology of the prepared nanofibers and nanocomposites, a transmission electron microscope (TEM) (TECNAI G2 20 S-TWIN, USA) operating at a voltage of 200 kV was used. The particle size distribution of the CNF suspension was measured by a nanoparticle size analyzer (Nanoplus-3).

4.2.3. Methods

4.2.3.1. Extraction of CNFs from factory tea waste

CNFs were extracted from WTFs following a previously reported method of alkali as well as acid hydrolysis and bleaching with minute changes [12]. To start with, the WTFs were washed with cold water several times to eliminate the dirt and other water soluble/washable impurities present in them and dried in an oven at 60 ℃. Afterward, 1 g of WTFs was treated with 100 mL of 20% NaOH for 4 hours (h) at 70 ℃ in order to remove lignin and facilitate the unbundling of the fibers. The process was duplicated by reducing the NaOH concentration by half. The residue was then washed repeatedly with distilled water to a neutral pH and further bleached with 7% H_2O_2 at 70 ℃ for 3 h, until the hemicellulose and lignin were eliminated, and a white mass was obtained. Further, the suspension was frozen with liquid nitrogen and crushed in a mortar and pestle for further unbundling of the microfibers into nanosized fibers. The obtained white mass was then subject to the third chemical treatment phase of acid hydrolysis in 50% acetic acid (50% water) for 3 h at 70 ℃. After neutralization by washing with water, the residue was dispersed in 50% aqueous DMSO for 3 h at 80 ℃ under magnetic stirring. The obtained CNF suspension in aqueous DMSO (50%) was sonicated (in a probe sonicator, model No. UP200S, Hielscher, Germany, with 0.5 cycles and 60% amplitude) for 20 minutes (min), and thereafter washed with water by repeated centrifugation. Subsequently, the solvent was changed from water to THF for future use. The process was repeated at least ten times to get a sufficient volume of CNF suspension as well as to confirm the repeatability of the procedure.

4.2.3.2. Functionalization of CNFs

Functionalization of the extracted CNFs was performed using TDI and EDA under a nitrogen atmosphere, using a method reported elsewhere [13] with minor modifications. CNF suspension (1 weight percent, wt%) in 30 mL dry THF was sonicated for 20 min to obtain a homogeneous dispersion. The suspension was then transferred into a three-neck round-bottom flask equipped with a reflux condenser, a nitrogen inlet, and a rubber septum. The required amount of TDI (30 wt% of CNFs, 0.17 mmol) was then injected dropwise into the suspension and magnetically stirred at room temperature (RT). After completion of the addition, the temperature was raised to 70 ± 3 ℃ and stirring was continued for 1.5 h to obtain isocyanate-pendant CNFs, as supported by FTIR spectral analysis (discussed later). The temperature of the reaction was then set back to RT, and an equimolar amount of EDA (0.011 mL, 0.17 mmol) was added drop by drop to the reaction mixture and heated to 65 ± 3 ℃. The reaction was continued for 2 h, after which the functionalized CNFs, codified as *f*-CNFs, were centrifuged with dry THF to remove the unreacted reactants and dispersed in THF for successive use.

The degree of substitution (DS) of *f*-CNF was calculated gravimetrically using a reported procedure and was repeated thrice [14]. It was calculated from the difference between the initial (W_{CNF}) and final weight ($W_{f\text{-}CNF}$) after modification and the molar masses of anhydrous glucose units (AGU, 162 g/mol), TDI (174.2 g/mol), and EDA (60.1 g/mol) as given in **Equation 4.2**.

$$DS = [(W_{f\text{-}CNF} - W_{CNF}) \times 162]/ [W_{CNF} \times (174.2 + 60.1)] \qquad \textbf{Equation 4.2}$$

4.2.3.3. Preparation of TAE

The bio-epoxy TAE was prepared by following the same process as detailed in **Chapter Two** under **Section 2.2.3.1**.

4.2.3.4. Fabrication of epoxy nanocomposite

The fabrication of the epoxy nanocomposite was carried out by the solution intercalation method, by physically mixing the TAE resin and dispersed *f*-CNF suspension. Briefly, 3 g of TAE was taken in a round bottom flask with a mechanical stirrer, and the required volume of *f*-CNFs was added to it. and the content was mixed at 70 ± 3 ℃ for 1 h. The homogenous mixture was then transferred to a 25-mL beaker with the required amount of poly(amido amine) hardener (50 wt% of TAE) and mixed properly, followed by vacuum

degassing to remove the excess solvent and trapped air bubbles. The mixture was then cast on glass plates and kept at RT until it became touch-free. The films were then cured at 100 °C and post-cured at 120 °C for specified period of time, to obtain the nanocomposite thermosets. The *f*-CNFs of 0.1, 0.2, and 0.3 wt % with respect to TAE were added, and the corresponding nanocomposite thermosets were labeled as *f*-CNF0.1/TAE, *f*-CNF0.2/TAE, and *f*-CNF0.3/TAE, respectively. For comparison purposes, a nanocomposite with 0.1 wt% bare CNFs was also prepared following the above-mentioned procedure and coded as CNF0.1/TAE.

4.2.3.5. Anticorrosion study

The anticorrosion properties of the nanocomposites were analyzed via PDP studies using a potentiostat (AUTOLAB PGSTAT302N, Metrohm, UK). The electrochemical system consisted of a silver electrode, a platinum wire, and coated plates as reference, counter, and working electrodes, respectively. The nanocomposite mixed with the hardener was applied to a steel plate of size 1 cm^2 and cured accordingly. The coated plates were then immersed in a 3.5% NaCl solution initially for 30 min, and their polarization curves were recorded, which was considered as the anticorrosion performance at 0^{th} day. Afterward, the substrates were dipped in the same electrolyte for 7 days and then studied.

The corrosion protection efficiency (PE) was measured for the nanocomposite coatings by utilizing the values of $I_{corr(bare)}$ (corrosion current of bare plate) and $I_{corr(coated)}$ (corrosion current of coated plates) using the following equation [15].

$$PE\ (\%) = [(I_{corr(bare)} - I_{corr(coated)})/\ I_{corr(bare)}] \times 100 \qquad \textbf{Equation 4.3}$$

Other studies, such as chemical resistance, biodegradation tests, etc., were performed following the standard procedures as described in **Chapter Two.**

4.3. Results and discussion

This work emphasized the extraction of CNFs for the first time from WTFs, which are abundant waste materials with potential utility. A reported method was followed for the extraction process, which was composed of chemical and mechanical treatments [12]. The extracted CNFs were further functionalized with urea-urethane linkages via a facile process, as shown in **Scheme 4.1**. The reactive isocyanate groups of TDI reacted with the hydroxyl groups of CNFs from one side, and the terminal isocyanate groups later reacted with EDA to form a urea linkage, as shown in the scheme. Thus, the functionalization of

CNFs introduced amine-blocked isocyanate groups on the surface of the nanofibers. The DS value obtained from the gravimetric method using **Equation 4.2** was found to be 0.032 ± 0.008. According to Fumagalli et al., the number of hydroxyl groups present on the surface of CNFs comprised only 5-27% of the total hydroxyl groups [14]. From this assumption, the DS value for typical surface functionalization of CNFs should not exceed 0.8. This alluded to the fact that the functionalization carried out in this work was also limited to the CNF surfaces only.

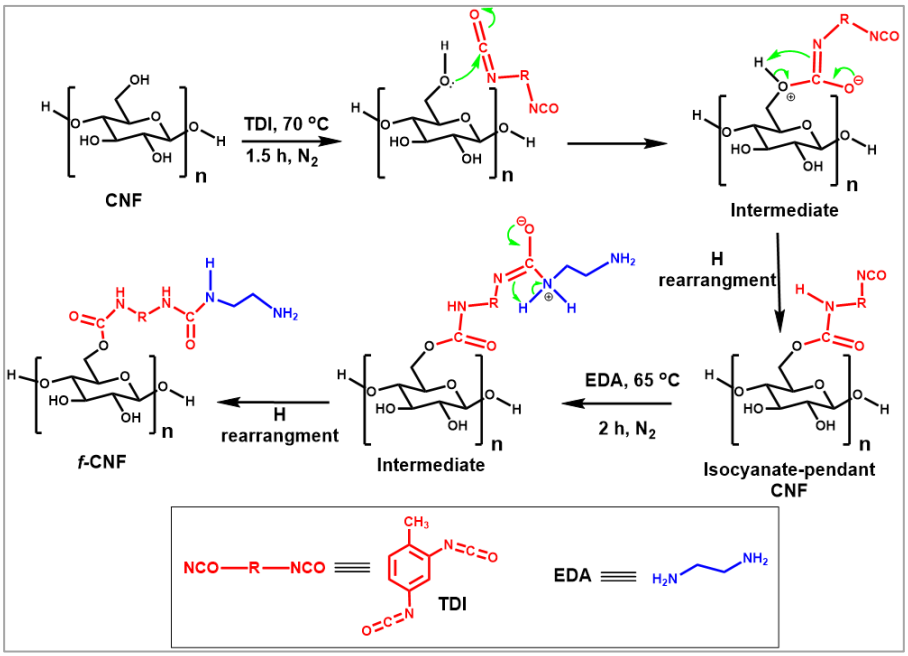

Scheme 4.1: Illustration of functionalization of CNFs with EDA blocked TDI

4.3.1. Chemical and morphological characterization of CNFs and *f*-CNFs

Figure 4.1(a) displays the FTIR spectra of CNFs, isocyanate-pendant CNFs, and *f*-CNFs. The stretching vibration of hydroxyl groups of CNFs appeared as a broad band around 3100-3600 cm^{-1} which also appeared in the spectrum of *f*-CNFs with a slightly lower intensity. The peak at 2931 cm^{-1} in both the spectra corresponds to aliphatic -CH_2 stretching, while peaks at 1636 cm^{-1}, 1427 cm^{-1}, and 892 cm^{-1} indicate the O-H bending vibration of absorbed water, -CH_2 scissoring vibration, and -C-O-C- linkage, respectively, which are typical characteristics of the cellulosic structure of CNFs [4, 16]. However, the isocyanate-pendant CNFs exhibited peaks at 2265 cm^{-1}, 1730 cm^{-1}, 1608 cm^{-1}, etc. that are the characteristics of free -N=C=O, urethane group, and aromatic C-H stretching vibrations indicating the presence of TDI on CNFs in an adequate amount. Moreover, the functionalization of CNFs with urea-urethane linkages resulted in the appearance of an

intense characteristic peak in *f*-CNFs at 1641 cm^{-1} arising from the -C=O stretching vibrations of secondary amide groups present in them, whereas the peak for -N=C=O

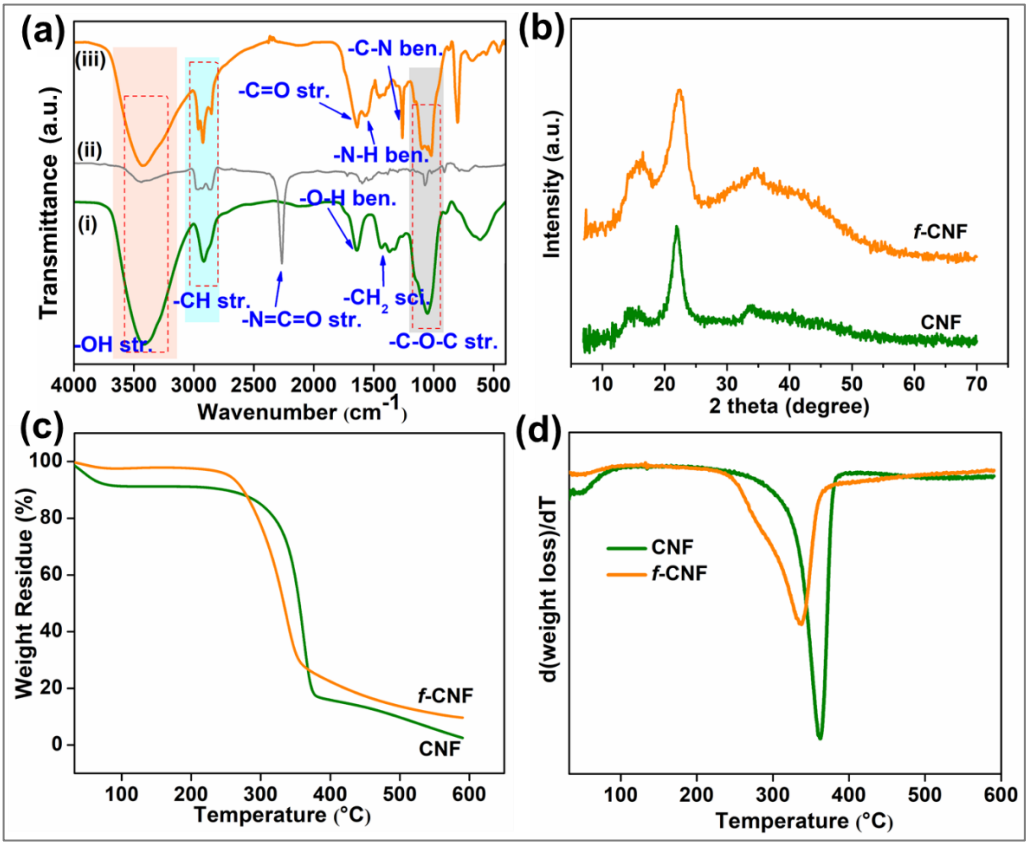

Figure 4.1: (a) FTIR spectra of (i) CNFs, (ii) isocyanate-pendant CNFs and (iii) *f*-CNFs, (b) XRD patterns of CNFs and *f*-CNFs and (c) TGA profiles, and (d) DTG curves of CNFs and *f*-CNFs

disappeared. While the peaks for the terminal amine groups were arising from EDA at 1571 cm^{-1} (N-H bending) and 1253 cm^{-1} for C-N stretching vibrations, as observed in similar reports [17]. To know the crystalline nature of CNFs and *f*-CNFs, the XRD patterns were recorded as presented in **Figure 4.1(b)**. The peak for 110-plane appeared at 15.0°, while the peak for 200-plane appeared at 21.9°. A CrI of 82.5% was reckoned for CNFs using **Equation 4.1**, which showed good crystallinity of the CNFs [7]. After functionalization with urea-urethane linkages, the XRD spectrum of *f*-CNFs showed a decrement in the intensity of the peaks, though the original structure of cellulose remained unaltered, as shown in the figure. This was obviously because of the chemical modification that covered the surface of the nanofibers imposing a slight amorphous nature on it and thereby lowering the crystalline character (CrI = 35.16%) [18]. However, the amorphous amine group and urea-urethane linkage containing pendant moieties disturbed the crystalline arrangement of the cellulose structure due to an increase in structural irregularity. Thus, more amorphous regions were detected on the surface of *f*-CNFs.

Additional broad peaks appeared at around 34.4° which is because of the amorphous nature of *f*-CNF, originating from the chemical modification. A similar XRD pattern was also observed in succinic anhydride-modified cellulose nanocrystals, where modification significantly lowered the crystallinity [19]. Bisla et al. extracted CNFs from rice straws and modified them with 1-methionine. The crystallinity of the modified CNFs was decreased due to the presence of amorphous sulfide and amide groups on the surface [20].

The thermogravimetric studies were performed to compare the thermostability of CNFs and *f*-CNFs, and the TGA profiles are presented in **Figure 4.1(c)** with DTG curves in **Figure 4.1(d)**. Three different regions were seen in both TGA profiles. In the case of CNFs, the degradation slowed down in region I (30 ℃ to 200 ℃) and resulted in only 10% weight loss, which was because of the evaporation of moisture absorbed on the CNF surfaces. Region II was noticed in the temperature range of 200 ℃ to 380 ℃, where a prominent degradation was recorded with an onset degradation temperature (T_{ON}) of 237 ℃ and a peak degradation temperature (T_p) of 361 ℃. This huge mass loss (83% mass loss with 17% residual weight) recorded was ascribed to the various chemical reactions such as oxidation, depolymerization, dehydration, and decarboxylation leading to the emission of small volatile substances [4]. In region III (380 ℃ to 600 ℃), the degradation slowed down, and a final residual weight of 2.5% was recorded. As stated by Lu et al., such high T_{ON} and T_p indicated a high crystallinity and good thermal stability of CNFs [21]. A similar degradation pattern was observed in *f*-CNFs. The initial 3% weight loss recorded in region I suggested lower moisture content in *f*-CNFs, presumably due to surface functionalization. Compared to CNFs, the degradation of *f*-CNFs started at a slightly lower temperature with T_{ON} at 225 ℃. However, a comparatively rapid degradation was noticed in *f*-CNFs, which originated from the thermal degradation of urea-urethane linkages formed between EDA, TDI, and hydroxyl groups of nanofibers [22]. Visibly, in **Figure 4.1(d)**, the T_p for this stage shifted to a lower temperature at 336 ℃ compared to CNFs as the crystallinity was significantly reduced due to functionalization. This might also have happened because of the small size of the fiber, which resulted in faster degradation of *f*-CNFs [23]. However, the weight residue of *f*-CNFs was slightly greater than that of CNFs, which might be aided by the enhanced nitrogen content in the former that facilitated higher weight residue content at temperatures above 400 ℃. Carbonaceous product formation is mostly due to the dehydration process, which is catalyzed by chemical groups (or their degradation products) that are attached to cellulose.

Furthermore, aromatic compounds (such as aromatic isocyanate) resulted in the formation of a higher amount of char compared to the carbohydrates present in CNFs. From these observations, it can be conferred that the functionalization has slightly lowered the thermal stability of the *f*-CNFs in comparison to CNFs. Similar results have also been reported by other studies where functionalization has lowered the thermal stability of the nanofibers [24].

The TEM images of CNFs and *f*-CNFs are presented in **Figure 4.2** at different magnifications. A well-dispersed web-like structure is observed in **Figure 4.2(b)** with nearly monodispersed CNFs spread all over the matrix, while bundling was observed in the case of *f*-CNFs, as seen in **Figure 4.2(e)**. This might have occurred due to highly polar functionalities present in the fiber surfaces that facilitate hydrogen bonding between the fibers. The diameters of the individual CNFs were found to be in the range of 20-120 nm, while those of *f*-CNFs ranged between 10-90 nm, as calculated from the TEM images using Image J software. The functionalization of CNFs resulted in a decrement in fiber diameter along with a significant enhancement of the surface roughness, as confirmed by **Figure 4.2(e)-(f)**. The particle distribution curves shown in **Figure 4.2(a)** and **(d)** obtained from the DLS study revealed the average diameters of CNFs and *f*-CNFs to be 130 nm and 107 nm, respectively, which were close to the results obtained from TEM images.

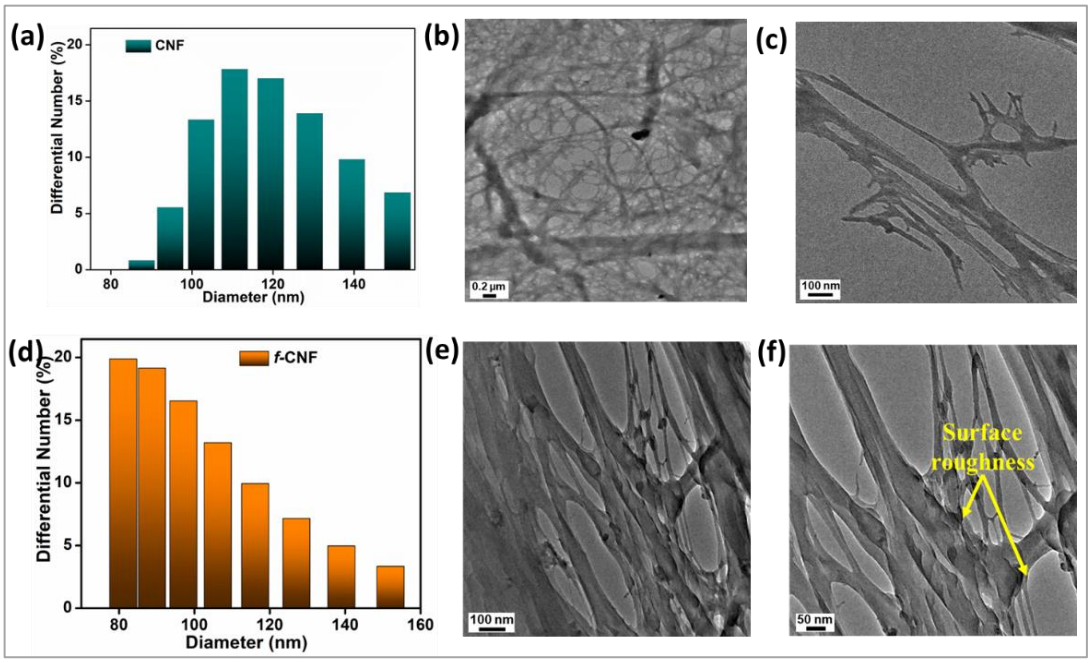

Figure 4.2: (a) and (d) size distribution of CNFs and *f*-CNFs obtained from DLS studies, TEM images of CNFs at (b) scale 200 nm and (c) scale 100 nm, and TEM images *f*-CNFs at scale (e) 100 nm, and (f) 50 nm

The elemental compositions determined from the EDS analysis for CNFs and *f*-CNFs are presented in **Figure 4.3(a)-(b)** with inset composition tables. CNFs possessed 49.73 atomic percent (at%) of carbon and 50.27 at% of oxygen. Ideally, cellulose possesses an equivalent amount of carbon and oxygen in its structure, which was reflected in the at% values. The slight increment in the oxygen content might be accredited to the absorbed water molecules on the surface of the fibers. Contrarywise, *f*-CNFs possessed 49.25 at% carbon, 49.53 at% oxygen, and 1.22 at% of nitrogen. The obvious presence of nitrogen in *f*-CNFs originating from the protruding amine groups on their surface supported the success of the modification process. **Figure 4.3(c)-(e)** shows the elemental mapping of *f*-CNFs, illustrating the distribution of carbon, oxygen, and nitrogen present on the surface. As shown in the mapping images, carbon and oxygen are present in equivalent amounts on the surface of *f*-CNFs, while the amount of nitrogen is relatively smaller. These mapping images further supported the presence of nitrogen-containing groups on the surface of the *f*-CNFs originating from the functionalization process. Bacterial cellulose surfaces modified with trimethoxysilane revealed similar behavior with functionalization restricted to the CNF's surface only [9].

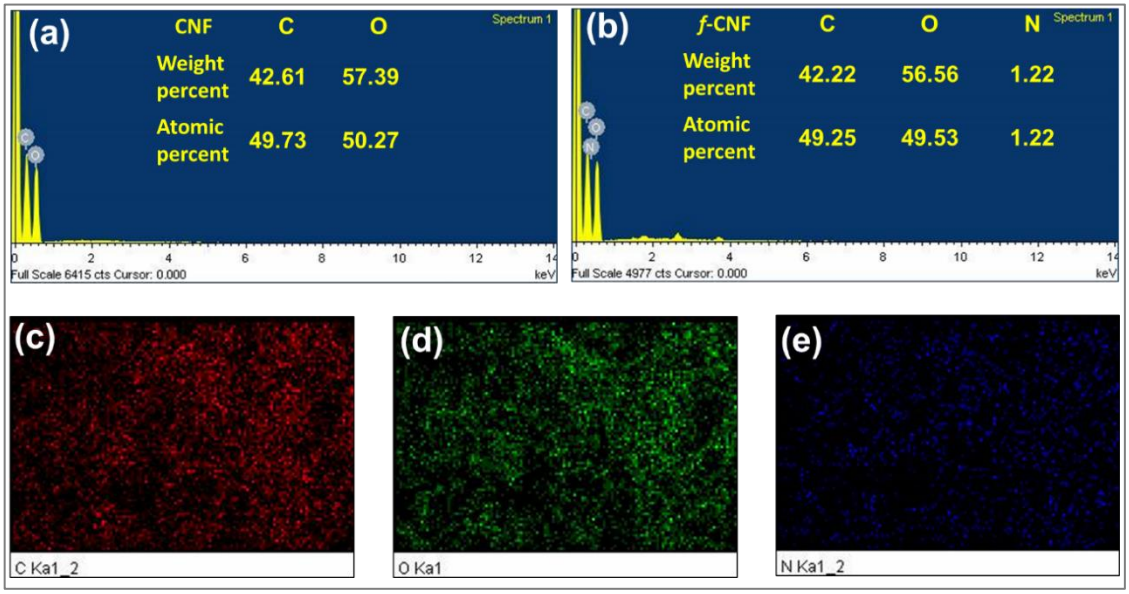

Figure 4.3: EDS spectra of (a) CNFs and (b) *f*-CNFs with inset composition tables, and elemental mapping of (c) carbon, (d) oxygen, and (e) nitrogen present in *f*-CNFs.

4.3.2. Fabrication and characterization of nanocomposite

An *ex-situ* fabrication technique was adopted for preparing the TAE/*f*-CNF nanocomposites. Initially, TAE and *f*-CNF suspensions in THF were physically mixed to

disperse the fibers throughout the resin. The addition of THF lowered the viscosity of the resin and facilitated a uniform amalgamation. While mixing, the terminal primary amine groups present in the *f*-CNFs were supposed to interact with the bio-based epoxy through covalent or non-covalent connections because of their propensity to attack the strained oxirane rings of the bio-based epoxy. Additionally, the polar groups present in *f*-CNFs would form hydrogen bonds with the epoxy group, resulting in a better interaction between the two [25]. On further adding the poly(amido amine) hardener during the curing process, residual epoxy rings would be utilized for further crosslinking and forming the three-dimensional thermosets. **Scheme 4.2** illustrates the possible interactive connections that happened between TAE and *f*-CNFs during the amalgamation at 70 °C and the curing process at higher temperatures.

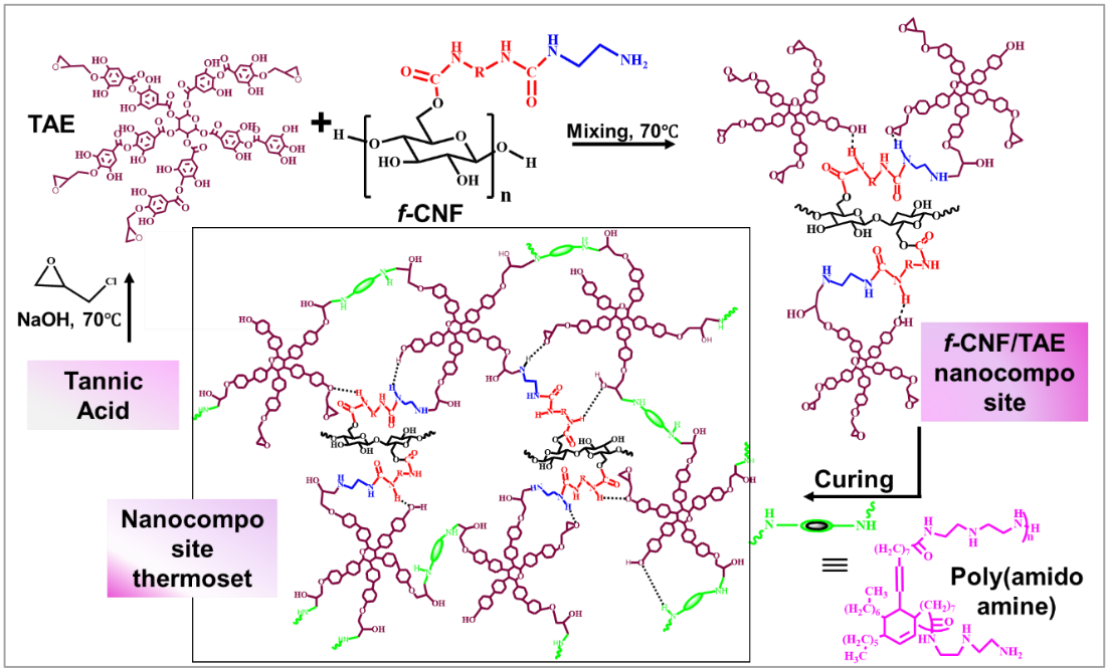

Scheme 4.2: Plausible mechanism of interaction between *f*-CNFs and TAE during the fabrication of nanocomposites and their thermosets

The curing parameters of the nanocomposites presented in **Table 4.1** showed that the time required for the *f*-CNF/TAE nanocomposites to become touch-free was far less than that of TAE. Similarly, the curing and post-curing times were lower than TAE and CNF0.1/TAE. This suggested the presence of extensive crosslinking between the *f*-CNFs and TAE resin initiated by covalent as well as non-covalent interactions between the hydroxyl and amine groups of *f*-CNFs, hydroxyl and epoxy groups of TAE, and the amine linkages of poly(amido amine).

Table 4.1: Curing parameters of the nanocomposite thermosets along with TAE at elevated temperature

Parameters	TAE	CNF0.1 /TAE	*f*-CNF0.1 /TAE	*f*-CNF0.2 /TAE	*f*-CNF0.3 /TAE
Touch free time at RT (h)	21 ± 2	20 ± 4	18 ± 3	15 ± 3	14 ± 2
Curing time at 100 ℃ (min)	60 ± 8	50 ± 6	50 ± 7	50 ± 5	50 ± 10
Post cure time at 120 ℃ (min)	7 ± 2	5 ± 4	5 ± 4	4 ± 4	4 ± 3

The ATR-FTIR spectra and XRD pattern recorded for the *f*-CNF/TAE and CNF/TAE nanocomposite thermosets are shown in **Figure 4.4**. From the FTIR spectra of TAE resin and the ATR-FTIR spectra of the cured thermosets shown in **Figure 4.4(a)**, it is visible that the characteristic peaks of oxirane ring stretching vibrations that appeared at around 850 cm^{-1} and 910 cm^{-1} in TAE resin were absent in the nanocomposite thermosets. This indicated that all the epoxy groups were consumed in the curing process via a reaction of epoxy-amine and epoxy-hydroxyl, as well as the homo-polymerization of epoxy [26]. The other peaks associated with -O-H stretching, -C-H stretching, -C=O stretching, -C(NH)=O stretching, -N-H bending, -C-N stretching, aromatic C-H deformation, etc. appeared at 3320 cm^{-1}, 2925 cm^{-1}, 1708 cm^{-1}, 1640 cm^{-1}, 1431 cm^{-1}, 1203 cm^{-1}, and 865 cm^{-1}, respectively, indicating the presence of diverse functionalities in the thermosets. However, the peak corresponding to hydroxyl groups in TAE resin was shifted from 3460 cm^{-1} to 3320 cm^{-1} in the TAE thermosets. Such shifting has occurred due to the ring opening of epoxy groups and the formation of new secondary hydroxyl groups in the thermosets during high-temperature curing [26]. The newly introduced amine linkages from the hardener also contributed to the same. The XRD patterns of the nanocomposite thermosets were recorded to understand the crystalline structure and the spectra are displayed in **Figure 4.4(b)**. All the thermosets exhibited a diffraction pattern similar to that of the neat epoxy, and the crystalline peaks corresponding to the nanofibers had no apparent effect on the nanocomposite thermosets due to very low loading [27]. Instead, broad amorphous peaks appeared at 22° and 43°, indicating the presence of proper interactions between the polymer and the fibers.

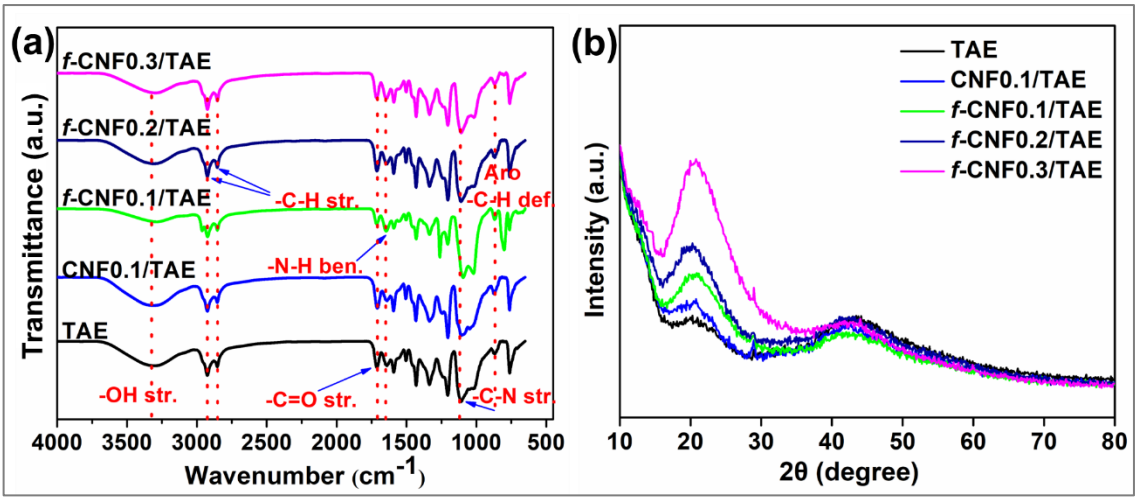

Figure 4.4: (a) ATR-FTIR spectra, and (b) XRD patterns of nanocomposite and TAE thermosets

4.3.3. Mechanical properties

The mechanical attributes of the prepared nanocomposites along with the neat TAE are reported in **Table 4.2**, while **Figure 4.5** shows the representative stress-strain profiles of the specimens. All four nanocomposites with CNFs and *f*-CNFs as reinforcing agents showed improvements in tensile strength compared to the neat epoxy. As perceived from the table, CNF0.1/TAE has an average tensile strength of 19.8 MPa, while the pristine epoxy showed a strength of 17.3 MPa. Interestingly, on incorporating even a sufficiently low wt% of *f*-CNFs (0.2 wt%) into the epoxy, the tensile strength of the nanocomposites soared up to 27.9 MPa (for *f*-CNF0.2/TAE) with a maximum enhancement of 61.1% compared to the pristine thermoset. However, with further increasing the loading of *f*-CNFs to 0.3 wt%, tensile strength dropped to 24.7 MPa, which might be because of the agglomerate formation among the fibers as the concentration of *f*-CNFs increased. Similar outcomes have been reported by Fazeli et al., where CNFs incorporating thermoplastic starch composites with 0.4% loading showed maximum tensile strength compared to 0.5% and 1.0% loading [28]. The improved strengths of these epoxy nanocomposites could be ascribed to the stiffness of the reinforcing agent evenly dispersed in the matrix that bolstered the latter [2]. Further, the improvement observed in the tensile strength values of *f*-CNF/TAEs compared to the CNF/TAE could be attributed to the presence of a greater number of cross-linkages in them because of *f*-CNFs which were facilitated by strong interfacial interactions with the matrix. The presence of pendant -NH_2 groups as well as urea linkages improved the interfacial interaction between the matrix and the fibers. The polar nitrogen and oxygen groups of *f*-CNFs either opened up the epoxy rings or formed

hydrogen bonds with the epoxy skeletal hydrogens, which improved the compatibility among the two components. **Table 4.3** represents the tensile strength of some recent

Table 4.2: Mechanical properties of the nanocomposite and TAE thermosets

Sample	Tensile strength (MPa)	Elongation at break (%)	Toughness (J/m^3)	Impact strength (kJ/m)	Scratch hardness (kg)
TAE	17.3 ± 0.65	33.7 ± 1.5	367.1 ± 29.1	19.6 ± 1.2	8 ± 0.5
CNF0.1/TAE	19.8 ± 0.8	48.8 ± 1.6	693.0 ± 26.1	22.5 ± 1.9	8 ± 0.5
***f*-CNF0.1/TAE**	21.1 ± 0.8	66.3 ± 6.7	458.1 ± 47.8	24.7 ± 2.3	8.5 ± 0.4
***f*-CNF0.2/TAE**	27.9 ± 3.7	50.4 ± 3.2	620.5 ± 49.4	31.3 ± 4.1	8.5 ± 0.5
***f*-CNF0.3/TAE**	24.7 ± 1.4	43.6 ± 4.5	518.8 ± 35.4	29.8 ± 2.9	8.5 ± 0.5

epoxy/cellulose nanocomposites. It can be observed that the enhancements recorded in the strength of most of the nanocomposites are lower than that of the studied one, which might be because of the upgraded matrix-nanofiber interactions in the latter. This reflected the superiority of the prepared nanocomposites over other reported ones with a very low loading of CNFs. Alternatively, the elongation at break values of the *f*-CNF/TAEs were considerably increased compared to the neat epoxy. The *f*-CNF0.1/TAE exhibited the highest elongation at break of 65.4% with a gradual decrease with further increasing the loading. These values were supposed to be affected by several counteracting factors, such as the dispersion of the nanofiller in the matrix, interfacial adhesion between them, and the volume fraction of the fibers. However, an expected reduction was observed in the elongation of CNF0.1/TAE. The toughness of the nanocomposite was calculated from the stress-strain profiles, and all the nanocomposites displayed much higher toughness values than the bare epoxy thermoset, as provided in **Table 4.2**.

The impact energies of the nanocomposites were measured, and the results are

demonstrated in **Table 4.2**. The incorporation of the nanofibers significantly enhanced the impact energies of the nanocomposites from 19.6 kJ/m for the host epoxy thermoset to

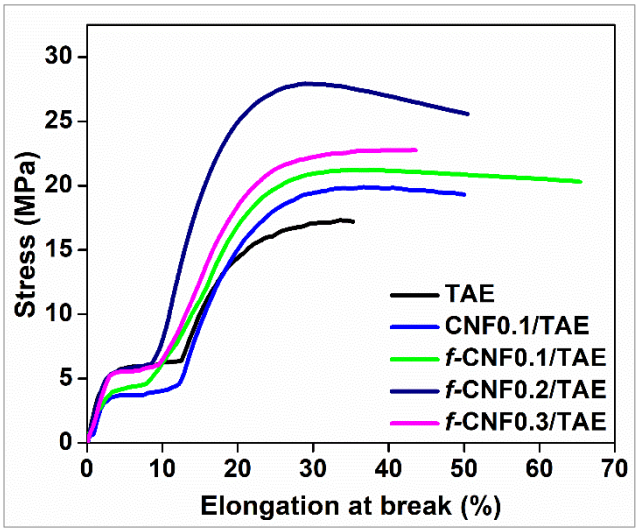

Figure 4.5: Stress-strain profiles of the thermosetting nanocomposites

31.3 kJ/m for *f*-CNF0.2/TAE. The introduction of these nanofibers facilitated the uniform propagation of impact energy through the matrix without damaging the substrate. Meanwhile, the *f*-CNF/TAE nanocomposite thermosets comparatively performed better than the CNF/TAE thermosets (22.5 kJ/m) because of the good interfacial interaction induced by the pendant amine groups present on the surface of the *f*-CNFs. In the case of *f*-CNF/TAEs, increasing the *f*-CNF loading to 0.3% resulted in a debasement in the impact strength. The formation of aggregates with higher loading might negatively affect energy absorption, resulting in a lower impact strength [29]. A CNF-reinforced poly(lactic acid)-based flame retardant nanocomposite also displayed a similar trend in impact strength [1]. The scratch hardness values of the nanocomposites also increased compared to the pristine, which was due to the high toughness of the nanocomposites.

4.3.4. Thermal properties

For assessing the thermal stabilities of the neat epoxy and its nanocomposite thermosets, TGA and DSC studies were carried out. **Table 4.4** displays the results obtained through the thermal degradation studies of the nanocomposite thermosets performed under a nitrogen atmosphere. All the nanocomposite thermosets exhibited similar degradation behavior as seen from the TGA and DTG profiles displayed in **Figure 4.6(a)** and **(b)**, respectively. As discussed earlier, the degradation of *f*-CNFs started at a temperature of

around 200 ℃, whereas the neat epoxy TAE displayed a T_{ON} of 210 ℃. As a result, the nanocomposites started degrading at a temperature below 210 ℃ and their TGA profiles appeared similar to those of TAE. The first- and second-stage T_p values also reflected a

Table 4.3: Summary of mechanical strengths of some recent epoxy/cellulose nanocomposite thermosets

Type of epoxy	Source of CNFs	Best loading (wt%)	Tensile strength (MPa)			Ref.
			Pure	Nano-composite	Enhancement (%)	
DGEBA	Banana fiber	5%	41.6	46.2	11.0	30
DGEBA	Softwood kraft pulp	0.75%	21.0	26.7	27.1	31
DGEBA	Sugarcane bagasse	3%	23.7	32	35.0	32
DGEBA	Modified MCC*	15%	46.6	63.5	36.2	33
DGEBA	Commercial CNFs	1%	24.8	50.4	103	34
Vanillin-based bio-epoxy	Tree bark	1%	32.9	59.5	80.8	26
Bio-based epoxy	**WTFs**	**0.3%**	**17.3**	**27.9**	**61.2**	**This work**

*MCC refers to microcrystalline cellulose

similar trend. This type of correlation was previously observed in a bacterial cellulose/epoxy nanocomposite [9]. The nanocomposites obtained by incorporating 5, 10, 20, and 30% bacterial cellulose into biobased epoxy diglycidyl ether diphenolate ethyl ester unveiled thermal stability lying in between the resin and the bacterial cellulose nano-filler [9]. Nonetheless, as seen in **Figure 4.6(b)**, the two different stages of degradation that appeared in the thermosets could be ascribed to the impairment of the different segments of the polymer chains present in the thermosets. The first degradation arose due to the depolymerization of TA, followed by damage to the ester linkages present in it. The second degradation, on the other hand, resulted from the breakage of the aromatic moieties

present in TAE, the aliphatic linkages resulting from the hardener, and the cycloaliphatic rings present in the nanofibers. The weight residues obtained after the completion of thermal degradation of the thermosets were found to increase with the increment in the loading of nanofiber, which agreed with reported studies [26]. According to Wang et al., the formation of a high amount of residual weight improved thermal stability by preventing the release of volatiles and generating a protective barrier on the surface of the polymer to lower the impairment [26]. Apparently, *f*-CNF0.3/TAE showed the highest thermal stability among all the nanocomposite thermosets. This was likely due to the presence of higher *f*-CNF loading, leading to agglomeration that acted as a barrier for heat transfer and retarded the degradation. In a study on TiO_2-incorporated epoxy nanocomposite, agglomeration of TiO_2 on the surface during degradation supposedly acted as a barrier and retarded the diffusion of heat and volatiles, thereby decreasing the rate of degradation [3].

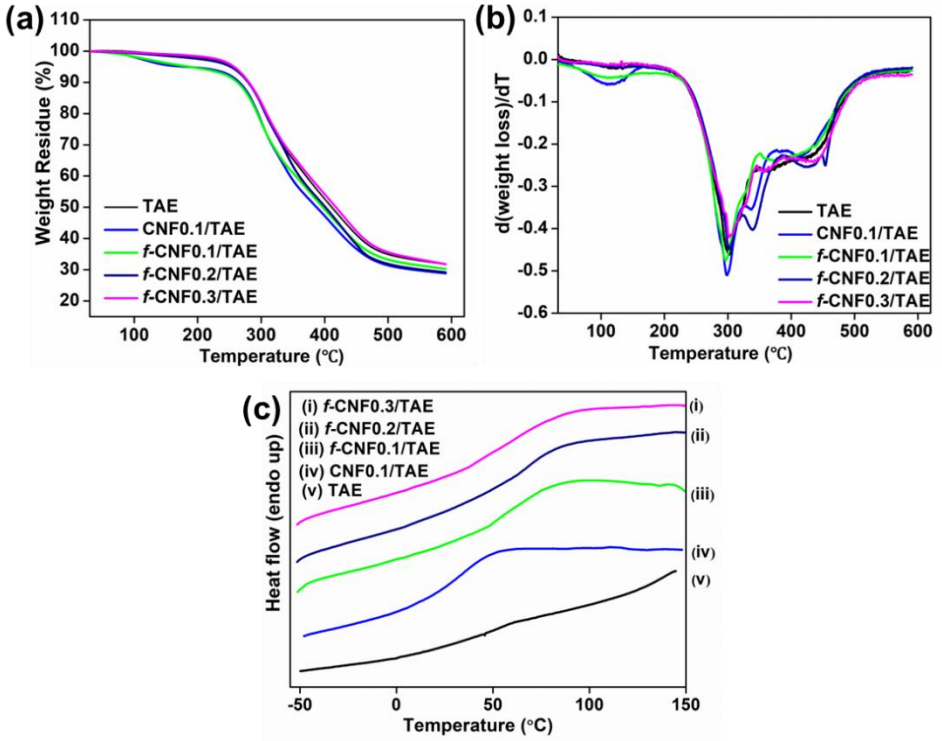

Figure 4.6: (a) TGA thermograms, (b) DTG curves, and (c) DSC profiles of the nanocomposite and TAE thermosets

The DSC curves, as presented in **Figure 4.6(c)**, highlighted the glass transition temperature (T_g) values of the bare TAE, CNF/TAE, and *f*-CNF/TAE thermosets at different loadings of the nano-reinforcing agent. The pure TAE showed a T_g value around 60 °C, while the incorporation of *f*-CNFs significantly increased the T_g to 86 °C for the highest loading of 0.3% in *f*-CNF0.3/TAE. Recently, Ji et al. reported epoxy nanocomposites containing Ag/MXene nanohybrid that exhibited higher T_g compared to

their parent epoxy, which further increased with increasing filler loading [35]. According to Liu et al., the T_g of a polymeric material was determined by the combined effects of the segmental motion of polymer chains, crosslinking, packing density, and entanglement constraints [36]. For the discussed nanocomposites, a high amount of crosslinking might have restricted the mobility of the polymer chains, which in turn augmented the T_g value.

Table 4.4: Thermal parameters of nanocomposites and TAE thermoset

Parameters	TAE	CNF0.1/ TAE	*f-*CNF0.1/ TAE	*f-*CNF0.2/ TAE	*f-*CNF0.3/ TAE
T_{ON} (°C)	210	194	202	202	204
1st stage T_p (°C)	305	298	296	303	303
2nd stage T_p (°C)	412	413	417	424	432
Weight residue at 600 °C (%)	31.73	28.8	30.26	29.18	3131.77
T_g (°C)	60	52	80	84	86

4.3.5. Anticorrosion study

A PDP study is an important electrochemical analysis tool for evaluating the anticorrosion performance of coatings [37]. In this study, a preliminary investigation on the anticorrosion performance of the fabricated nanocomposites was carried out by immersing the coated metal plates in a 3.5% NaCl solution for 7 days. The Tafel plots of the coated plates obtained at the 0th and 7th days of immersion are presented in **Figure 4.7(a)** and **(b)**, respectively, and the parameters obtained by extrapolation of the Tafel plots to intersection points are presented in **Table 4.5**.

The results presented in **Table 4.5** reflected that compared to the bare mild steel plate, all the nanocomposites and the pristine epoxy coated plates exhibited lower I_{corr} values, higher E_{corr} values, lower corrosion rates (r_{corr}, measured in mils per year, mpy), and higher polarization resistance (R_p) values, indicating better anticorrosive behavior of

the coatings. However, when the nanocomposites and TAE-coated plates were considered, the nanocomposite-coated plates revealed better anticorrosion performance compared to the bare epoxy ones. The E_{corr} and I_{corr} values of TAE-coated plates were found to be -0.8087 V and 9.54×10^{-8} A.cm^{-2}, respectively, with a PE of 99.54%. Alternatively,

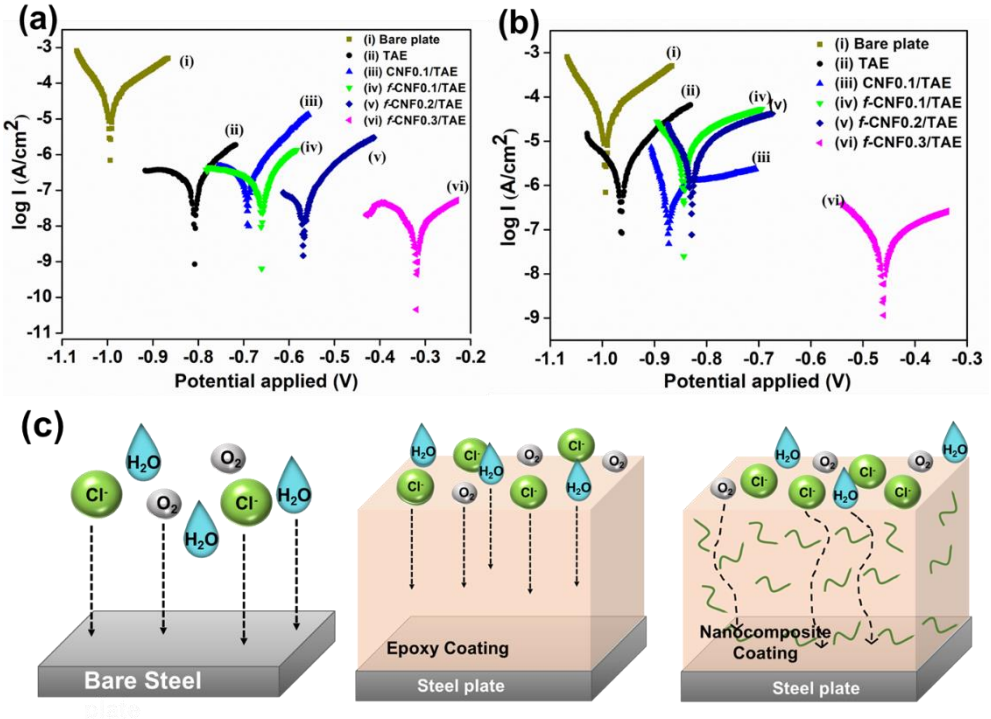

Figure 4.7: Tafel plots for coated and uncoated samples at (a) 0th and (b) 7th day immersion time, and (c) schematic representation of corrosion protection mechanism of nanocomposite coatings

nanocomposite-coated plates showed significantly better E_{corr} and I_{corr} values than TAE. Further, the corrosion inhibiting ability increased with the increase of the nano-reinforcing agent loading, and E_{corr}, R_p, and PE values gradually increased, while I_{corr} values, as well as corrosion rates, gradually decreased from CNF0.1/TAE to *f*-CNF0.3/TAE. Specifically, the inclusion of 0.3% *f*-CNFs reduced the I_{corr} to 9.65×10^{-9} A.cm^{-2}, while the E_{corr} value increased up to -0.3191 V with a PE of 99.95%, indicating the investigated *f*-CNF0.3/TAE nanocomposite as an effective anticorrosive coating for the mild steel plates. The R_p value for the same was found to be the highest, 7.51×10^5 Ω, and the corrosion rate was the lowest (7.63×10^{-9} mpy) among all the nanocomposites. On immersing the steel plates for 7 days in the corrosive medium, a significant decrement was noticed in the anticorrosion ability of the epoxy and nanocomposites, as shown in **Figure 4.7(b)**. All the substrates, excluding the *f*-CNF0.3/TAE-coated substrates suffered corrosion as their E_{corr} shifted to electronegative values and their I_{corr} shifted to more positive values. As perceived from

Table 4.5, TAE-coated plates suffered the most, when exposed for a long time to the corrosive medium, as their PE dropped from 99.54% to

Table 4.5: Electrochemical parameters of TAE and nanocomposites obtained from Tafel plots

Sample	Time (days)	E_{corr} (V)	I_{corr} ($A.cm^{-2}$)	R_p (Ω)	r_{corr} (mpy)	PE%
Bare plate	0	-0.9952	2.11×10^{-5}	233.85	2.45×10^{-2}	-
TAE	0	-0.8087 ± 0.051	(9.54 ± 0.14)×10^{-8}	(1.34 ± 0.15)×10^{4}	(1.10 ± 0.30) ×10^{-3}	99.54
	7	-0.9644 ± 0.006	(3.86±0.13) ×10^{-6}	(6.44 ± 0.54)×10^{3}	(4.49 ± 0.95)×10^{-2}	81.17
CNF0.1/TAE	0	-0.6976 ± 0.078	(7.00 ± 0.17)×10^{-8}	(8.94 ± 1.20)×10^{4}	(8.13 ± 1.10)×10^{-4}	99.66
	7	-0.8741 ± 0.023	(9.16 ± 0.34)×10^{-7}	(1.61 ± 0.26)×10^{4}	(1.06 ± 0.15)×10^{-3}	95.65
***f*-CNF0.1/TAE**	0	-0.6618 ± 0.008	(1.21 ± 0.59)×10^{-8}	(1.66 ± 0.23)×10^{5}	(1.40 ± 0.40)×10^{-4}	99.84
	7	-0.8324 ± 0.021	(9.75 ± 0.09)×10^{-7}	(5.94 ± 0.62)×10^{4}	(6.12 ± 0.77)×10^{-3}	95.37
***f*-CNF0.2/TAE**	0	-0.5692 ± 0.075	(5.99 ± 0.15)×10^{-9}	(4.37 ± 0.48)×10^{5}	(6.99 ± 0.94)×10^{-5}	99.87
	7	-0.8372 ± 0.006	(2.48 ± 0.45)×10^{-7}	(8.13 ± 0.46)×10^{4}	(2.88 ± 0.50)×10^{-4}	98.82
***f*-CNF0.3/TAE**	0	-0.3191 ± 0.057	(9.65 ± 0.65)×10^{-9} ±	(2.86 ± 0.32)×10^{8}	(7.63 ± 1.22)×10^{-9}	99.95
	7	-0.4614 ± 0.043	(3.80 ± 0.87)×10^{-8}	(7.51 ± 0.51)×10^{5}	(4.11 ± 0.80)×10^{-5}	99.81

81.14%. Alternatively, the PE of *f*-CNF0.3/TAE changed from 99.95% to 99.81% with only a 0.14% decrease after immersion in a 3.5% NaCl solution, implying its good corrosion resistance behavior. The optimum addition of 0.3% *f*-CNF and the formation of agglomerates in the matrix might be accountable for such good performance.

During the immersion period, when the steel plate (which acts as the anode) comes in contact with the corrosive electrolyte, the anode undergoes metal dissolution, while the cathode experiences reduction of oxygen, as shown below [38].

At anode, $Fe \rightarrow Fe^{2+} + 2e^-$ **Equation 4.4**

At cathode, $O_2 + H_2O + 4e^- \rightarrow 4OH^-$ **Equation 4.5**

The electropositive iron ions can then react with the hydroxyl ions to produce iron oxides or conventional rust. In the case of the bare metal plate, which is directly exposed to the electrolyte, the corrosive ions can easily cause the dissolution of the metal, initiating severe corrosion in it, as shown in **Figure 4.7(c)**. When a coating is applied over the metal surface, the electrolyte is restricted from direct contact with the metal plate. Rather, the electrolyte is first absorbed in the coating, and the corrosive ions ingress through the coating to the coating-metal interface and finally interact with the metal [15]. As a result, the process of corrosion slows down. Coatings with high strength, dense crosslinking, and reinforced with nano- or micro-fillers can create a protective barrier over metal surfaces, producing tougher transportation pathways for the corrosive ions that further slowdown the damage [39]. The same might have happened with the studied nanocomposites, as their high crosslinking density and the presence of nano-reinforcing agents retarded the movement of the corrosive moieties like water and chloride ions by inducing a torturous path for them and, hence, impeded the damage at the steel surface. The possible representation of the corrosion protection mechanism is presented in **Figure 4.7(c)**.

Interestingly, while looking at the literature, it is found that CNFs have been mostly employed as nanocarriers for releasing corrosion inhibitors instead of directly applying them as corrosion-protecting agents. Tanvir et al. immobilized epoxy and amine curing agents individually on CNFs and applied them to metal substrates to study their self-healing and anticorrosion activities [40]. Recently, Devadasu et al. loaded benzotriazole into nanocellulose derived from teak sawdust and reinforced it with an epoxy/polyamide system that showed good corrosion inhibition in mild steel after 72 h of immersion in 3% aqueous NaCl [41]. The reinforcement of 2, 4, and 6 wt% benzotriazole-loaded nanocellulose lowered the I_{corr} from 1.304×10^{-6} to 2.472×10^{-8} to 2.688×10^{-8} A.cm^2, while the E_{corr} shifted from -0.682 to -0.498 to -0.475 V, respectively [41]. The fabricated material in this work exhibited similar I_{corr} and E_{corr} values without bearing any corrosion

inhibitor species in CNFs. However, for obtaining a clear picture, a more detailed study needs to be performed, which falls in the future prospects.

4.3.6. Chemical resistance

For coating-based applications, it becomes vital for the studied materials to show good chemical resistance, which is generally monitored by the extent of physico-chemical changes occurring on exposure to different environmental agents [37]. For this purpose, the nanocomposites were subject to mild acidic (pH 4.4), alkaline (pH 9), and electrolytic (5% NaCl) aqueous solutions as well as organic solvent (5% aqueous EtOH) for 15 days at RT and afterward, their gravimetric changes were recorded. The weight loss percentages of the nanocomposites listed in **Table 4.6** revealed good resistivity toward the abovementioned environments. From the table, it is also visible that the presence of the nanofibers conserved the integrity of the nanocomposites to some extent compared to the neat epoxy thermoset. The observed deterioration could be attributed to the physical degradation, which was caused by the diffusion of acid, alkali, ions, or solvent species into the free spaces present inside the polymer network. This resulted in swelling of the specimens [42]. Subsequently, chemical degradation came into play when these penetrant species adhered to the polymer chains and disturbed the crosslinking by hydrolyzing, oxidizing, or breaking the epoxy linkages [42]. However, with the inclusion of nanofibers, the extra voids were removed to some extent due to an increment in the crosslinking density. This further lowered the segmental mobility of the polymer chains, thereby inhibiting the penetration of solute molecules through the thermosets. Consequently, nanocomposites with *f*-CNFs showed lower weight loss compared to CNF0.1/TAE with bare CNFs with the same loading, which, in turn, was lower than TAE thermoset. Moreover, due to the uniform dispersion of *f*-CNFs without agglomeration, and enhanced crosslinking induced by pendant NH_2 groups, *f*-CNF0.2/TAE was least affected by the chemical environments and thus showed better resistivity compared to *f*-CNF0.1/TAE and *f*-CNF0.3/TAE.

4.3.7. Biodegradation behavior

The prime criterion for a bio-derived polymeric material to serve as a sustainable alternative to petroleum-based ones is their biodegradability in the environment. Polymeric materials that can be easily discarded into the environment after their service life and have the ability to break down into smaller harmless moieties without liberating

noxious chemicals have been increasingly drawing attention from society [43]. Giving consideration to these facts, the TAE, *f*-CNF/TAE, and CNF/TAE thermosets were subject to accelerated biodegradation triggered by the *B. subtilis* bacterial strain. The growth of the bacterial solutions in the presence of the nanocomposites was monitored by measuring

Table 4.6: Weight loss (%) of the thermosetting nanocomposites after the chemical resistance test

Sample	pH = 9.0	pH = 4.4	5% NaCl	5% EtOH
TAE	4.79 ± 0.9	5.12 ± 1.2	3.93 ± 1.0	2.88 ± 0.05
CNF0.1/TAE	3.94 ± 0.4	3.41 ± 1.6	2.93 ± 0.7	2.19 ± 0.06
***f*-CNF0.1/TAE**	3.84 ± 0.4	3.20 ± 0.4	2.36 ± 0.7	1.43 ± 0.1
***f*-CNF0.2/TAE**	2.78 ± 0.2	2.06 ± 0.1	$1.98 \times 10^{-3} \pm 0.0$	$8.55 \times 10^{-3} \pm 0.0$
***f*-CNF0.3/TAE**	3.60 ± 0.8	2.58 ± 0.4	1.20 ± 0.0	1.15 ± 0.0

the optical density (OD) of the bacterial solutions at regular intervals. **Figure 4.8(a)** displays the OD curves of the nanocomposite thermosets along with the pristine epoxy thermoset. As apparent from the figure, all the solutions with nanocomposite films showed higher bacterial growth compared to TAE, which might be because of the presence of CNFs in the former cases. However, compared to *f*-CNF/TAE nanocomposites, CNF0.1/TAE showed good bacterial colonization. The presence of exposed hydroxyl groups in CNFs might be accountable for such enhanced bacterial growth, which increased the propensity for degradation. Conversely, surface functionalization has reduced the rate of degradation of *f*-CNF/TAE nanocomposites by lowering the concentration of their surface hydroxyl groups in *f*-CNFs. The weight loss (%) values of the thermosets recorded after 30 days of bacterial incubation are displayed in **Figure 4.8(b)**. As reflected in the results, all the nanocomposites suffered higher weight loss than TAE, with the highest weight loss of 9.3% being recorded for CNF0.1/TAE, which resembled the results obtained from the OD curves. Both the bacterial growth and weight loss results justified the conclusion that the extent of degradation was proportional to the *f*-CNF loading in the

nanocomposites. According to Dutta and Karak, during bacterial degradation, the microorganisms present in the system liberated specific enzymes that hydrolyzed the labile

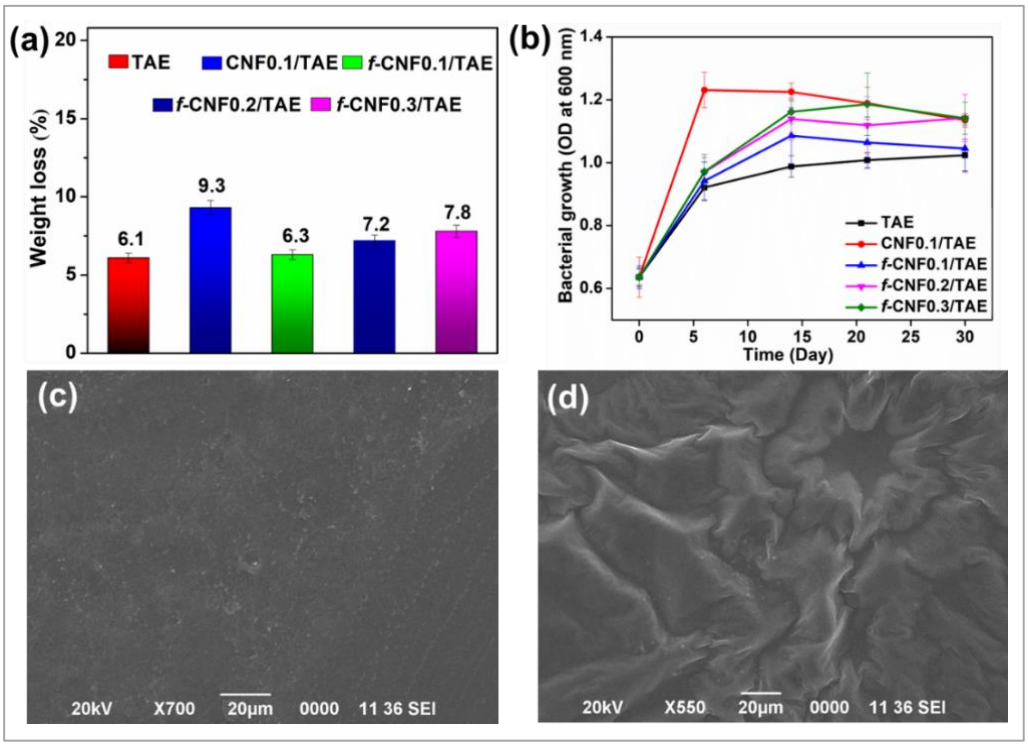

Figure 4.8: (a) Bacterial growth curves in terms of OD presented as a function of time, (b) weight loss (%) of the nanocomposites along with TAE recorded after the bacterial degradation, (c) SEM images *f*-CNF0.3/TAE as control before and (d) after biodegradation

polymeric linkages (e.g., ester linkage) of the thermosets [12]. This hydrolysis of the polymeric fragments caused surface erosion in the thermosets, which could be evident from the SEM micrograph presented in **Figure 4.8(d)**. As shown in **Figure 4.8(c)**, the *f*-CNF0.3/TAE thermoset has a smooth surface before biodegradation. However, after the commencement of the bacteria-triggered degradation, the surface of *f*-CNF0.3/TAE appeared rough, and significant erosion was elicited, leaving crests and troughs in the surface of the thermoset as shown in **Figure 4.8(d)**.

4.4. Conclusion

This work demonstrated a simple and sustainable process for the extraction of CNFs from potential biowastes like WTFs through facile chemical and mechanical treatments. The obtained CNFs were further successfully modified with pendant amine-blocked isocyanate to introduce urea-urethane linkages with pendant amine groups over the surface. The structural and morphological analyses of the *f*-CNFs revealed the presence of nitrogen-rich chemical linkages over the surface of the *f*-CNFs that influenced their crystallinity and

thermal behavior. Subsequently, the *f*-CNFs were incorporated in the bio-based epoxy like TAE for the fabrication of *f*-CNF/TAE nanocomposites through a physical amalgamation technique. Incorporation of *f*-CNFs at very low concentrations resulted in considerable enhancements in the mechanical performance and thermal properties of the nanocomposites, as well as good anticorrosion activity when applied to metal substrates, enabling their wide application in coating industries. To conclude, the study provided a facile approach for the design of surface-tailored CNFs for the fabrication of high-performance benign epoxy nanocomposites with potential application as an anticorrosive coating.

References

[1] Feng, J., Sun, Y., Song, P., Lei, W., Wu, Q., Liu, L., Yu, Y., and Wang, H. Fire-resistant, strong, and green polymer nanocomposites based on poly (lactic acid) and core–shell nanofibrous flame retardants. *ACS Sustainable Chemistry & Engineering*, 5(9):7894-7904, 2017.

[2] Li, K., Clarkson, C. M., Wang, L., Liu, Y., Lamm, M., Pang, Z., Zhou, Y., Qian, J., Tajvidi, M., Gardner, D. J., and Tekinalp, H. Alignment of cellulose nanofibers: Harnessing nanoscale properties to macroscale benefits. *ACS Nano*, 15(3):3646-3673, 2021.

[3] Nagarajan, K. J., Balaji, A. N., and Ramanujam, N. R. Extraction of cellulose nanofibers from *cocos nucifera var aurantiaca* peduncle by ball milling combined with chemical treatment. *Carbohydrate Polymers*, 212:312-322, 2019.

[4] Ravindran, L., Sreekala, M. S., and Thomas, S. Novel processing parameters for the extraction of cellulose nanofibres (CNF) from environmentally benign pineapple leaf fibres (PALF): Structure-property relationships. *International Journal of Biological Macromolecules*, 131:858-870, 2019.

[5] Wang, Z., Gnanasekar, P., Sudhakaran Nair, S., Farnood, R., Yi, S., and Yan, N. Biobased epoxy synthesized from a vanillin derivative and its reinforcement using lignin-containing cellulose nanofibrils. *ACS Sustainable Chemistry & Engineering*, 8(30):11215-11223, 2020.

[6] Zhao, J., Li, Q., Zhang, X., Xiao, M., Zhang, W., and Lu, C. Grafting of polyethylenimine onto cellulose nanofibers for interfacial enhancement in their epoxy nanocomposites. *Carbohydrate Polymers*, 157:1419-1425, 2017.

[7] Niu, X., Liu, Y., Song, Y., Han, J., and Pan, H. Rosin modified cellulose nanofiber as a reinforcing and co-antimicrobial agent in polylactic acid/chitosan composite film for food packaging. *Carbohydrate Polymers*, 183:102-109, 2018.

[8] Siqueira, G., Bras, J., and Dufresne, A. New process of chemical grafting of cellulose nanoparticles with a long chain isocyanate. *Langmuir*, 26(1):402-411, 2010.

[9] Yue, L., Liu, F., Mekala, S., Patel, A., Gross, R. A., and Manas-Zloczower, I. High performance biobased epoxy nanocomposite reinforced with a bacterial cellulose nanofiber network. *ACS Sustainable Chemistry & Engineering*, 7(6):5986-5992, 2019.

[10] Ke, W. T., Chiu, H. L., and Liao, Y. C. Multifunctionalized cellulose nanofiber for water-repellent and wash-sustainable coatings on fabrics. *Langmuir*, 36(28):8144-8151, 2020.

[11] Segal, L. G. J. M. A., Creely, J. J., Martin Jr, A. E., and Conrad, C. M. An empirical method for estimating the degree of crystallinity of native cellulose using the X-ray diffractometer. *Textile Research Journal*, 29(10):786-794, 1959.

[12] Dutta, G. K. and Karak, N. Waste brewed tea leaf derived cellulose nanofiber reinforced fully bio-based waterborne polyester nanocomposite as an environmentally benign material. *RSC Advances*, 9(36):20829-20840, 2019.

[13] Thakur, S. and Karak, N., Ultratough, ductile, castor oil-based, hyperbranched, polyurethane nanocomposite using functionalized reduced graphene oxide. *ACS Sustainable Chemistry & Engineering*, 2(5):1195-1202, 2014.

[14] Fumagalli, M., Ouhab, D., Boisseau, S. M., and Heux, L. Versatile gas-phase reactions for surface to bulk esterification of cellulose microfibrils aerogels. *Biomacromolecules*, 14(9):3246-3255, 2013.

[15] Dutta, G. K. and Karak, N. Bio-based waterborne polyester/cellulose nanofiber-reduced graphene oxide–zinc oxide nanocomposite: An approach towards sustainable mechanically robust anticorrosive coating. *Cellulose*, 29(3):1679-1703, 2022.

[16] Yang, X., Ku, T. H., Biswas, S. K., Yano, H., and Abe, K. UV grafting: Surface modification of cellulose nanofibers without the use of organic solvents. *Green Chemistry*, 21(17):4619-4624, 2019.

[17] Haq, F., Kiran, M., Chinnam, S., Farid, A., Khan, R. U., Ullah, G., Aljuwayid, A. M., Habila, M. A., and Mubashir, M. Synthesis of bioinspired sorbent and their

exploitation for methylene blue remediation. *Chemosphere*, 321:138000-138013, 2023.

[18] Jonoobi, M., Harun, J., Mathew, A. P., Hussein, M. Z. B., and Oksman, K. Preparation of cellulose nanofibers with hydrophobic surface characteristics. *Cellulose*, 17:299-307, 2010.

[19] Aziz, T., Farid, A., Chinnam, S., Haq, F., Kiran, M., Alothman, Z. A., Aljuwayid, A. M., Habila, M. A., and Akhtar, M. S. Synthesis, characterization and adsorption behavior of modified cellulose nanocrystals towards different cationic dyes. *Chemosphere*, 321:137999-138009, 2023.

[20] Bisla, V., Rattan, G., Singhal, S., and Kaushik, A. Green and novel adsorbent from rice straw extracted cellulose for efficient adsorption of Hg (II) ions in an aqueous medium. *International Journal of Biological Macromolecules*, 161:194-203, 2020.

[21] Lu, Y., Tao, P., Zhang, N., and Nie, S. Preparation and thermal stability evaluation of cellulose nanofibrils from bagasse pulp with differing hemicelluloses contents. *Carbohydrate Polymers*, 245:116463-116471, 2020.

[22] Coutinho, F. M., Delpech, M. C., Alves, T. L., and Ferreira, A. A. Degradation profiles of cast films of polyurethane and poly (urethane-urea) aqueous dispersions based on hydroxy-terminated polybutadiene and different diisocyanates. *Polymer Degradation and Stability*, 81(1):19-27, 2003.

[23] Zhang, W., Zhang, X., Ren, S., Dong, L., Ai, Y., Lei, T., and Wu, Q. Lignin containing cellulose nanofiber based nanopapers with ultrahigh optical transmittance and haze. *Cellulose*, 30:5967-5985, 2023.

[24] Huang, P., Zhao, Y., Kuga, S., Wu, M., and Huang, Y., A versatile method for producing functionalized cellulose nanofibers and their application. *Nanoscale*, 8(6):3753-3759, 2016.

[25] Saikia, A. and Karak, N. Renewable resource based thermostable tough hyperbranched epoxy thermosets as sustainable materials. *Polymer Degradation and Stability*, 135:8-17, 2017.

[26] Wang, Z., Gnanasekar, P., Sudhakaran Nair, S., Farnood, R., Yi, S., and Yan, N. Biobased epoxy synthesized from a vanillin derivative and its reinforcement using lignin-containing cellulose nanofibrils. *ACS Sustainable Chemistry & Engineering*, 8(30):11215-11223, 2020.

[27] Li, J., Yan, Q., and Cai, Z. Fabrication and characterization of emulsified and freeze-dried epoxy/cellulose nanofibril nanocomposite foam. *Cellulose*, 26:1769-1780, 2019.

[28] Fazeli, M., Keley, M., and Biazar, E. Preparation and characterization of starch-based composite films reinforced by cellulose nanofibers. *International Journal of Biological Macromolecules*, 116:272-280, 2018.

[29] Padinjakkara, A., Scarinzi, G., Santagata, G., Malinconico, M., Razal, J. M., Thomas, S., and Salim, N. V. Enhancement of adhesive strength of epoxy/carboxyl-terminated poly (butadiene-co-acrylonitrile) nanocomposites using waste hemp fiber-derived cellulose nanofibers. *Industrial & Engineering Chemistry Research*, 59(23):10904-10913, 2020.

[30] Pandurangan, M. T. and Kanny, K. Study of curing characteristics of cellulose nanofiber-filled epoxy nanocomposites. *Catalysts*, 10(8):831-845, 2020.

[31] Saba, N., Mohammad, F., Pervaiz, M., Jawaid, M., Alothman, O. Y., and Sain, M. Mechanical, morphological and structural properties of cellulose nanofibers reinforced epoxy composites. *International Journal of Biological Macromolecules*, 97:190-200, 2017.

[32] Wongjaiyen, T., Brostow, W., and Chonkaew, W. Tensile properties and wear resistance of epoxy nanocomposites reinforced with cellulose nanofibers. *Polymer Bulletin*, 75:2039-2051, 2018.

[33] Lou, G., Ma, Z., Dai, J., Bai, Z., Fu, S., Huo, S., Qian, L., and Song, P. Fully biobased surface-functionalized microcrystalline cellulose via green self-assembly toward fire-retardant, strong, and tough epoxy biocomposites. *ACS Sustainable Chemistry & Engineering*, 9(40):13595-13605, 2021.

[34] Vidakis, N., Petousis, M., Michailidis, N., Kechagias, J. D., Mountakis, N., Argyros, A., Boura, O., and Grammatikos, S. High-performance medical-grade resin radically reinforced with cellulose nanofibers for 3D printing. *Journal of the Mechanical Behavior of Biomedical Materials*, 134:105408, 2022.

[35] Ji, C., Wang, Y., Ye, Z., Tan, L., Mao, D., Zhao, W., Zeng, X., Yan, C., Sun, R., Kang, D. J., and Xu, J. Ice-templated MXene/Ag–epoxy nanocomposites as high-performance thermal management materials. *ACS Applied Materials & Interfaces*, 12(21):24298-24307, 2020.

[36] Liu, C., Chen, T., Yuan, C. H., Song, C. F., Chang, Y., Chen, G. R., Xu, Y. T., and Dai, L. Z. Modification of epoxy resin through the self-assembly of a surfactant-

like multi-element flame retardant. *Journal of Materials Chemistry A*, 4(9):3462-3470, 2016.

[37] Sheng, X., Mo, R., Ma, Y., Zhang, X., Zhang, L., and Wu, H. Waterborne epoxy resin/polydopamine modified zirconium phosphate nanocomposite for anticorrosive coating. *Industrial & Engineering Chemistry Research*, 58(36):16571-16580, 2019.

[38] Joseph, A., John Mathew, K. P., and Vandana, S. Zirconium-doped ceria nanoparticles as anticorrosion pigments in waterborne epoxy–polymer coatings. *ACS Applied Nano Materials*, 4(1):834-849, 2020.

[39] Bhat, S. I. and Ahmad, S. Castor oil-TiO_2 hyperbranched poly(ester amide) nanocomposite: A sustainable, green precursor-based anticorrosive nanocomposite coatings. *Progress in Organic Coatings*, 123:326-336, 2018.

[40] Tanvir, A., El-Gawady, Y. H., and Al-Maadeed, M. Cellulose nanofibers to assist the release of healing agents in epoxy coatings. *Progress in Organic Coatings*, 112:127-132, 2017.

[41] Devadasu, S., Sonawane, S. H., and Suranani, S. Self-healing corrosion inhibition coatings with pH-responsive activity by incorporation of nano cellulose in two pack epoxy polyamide system. *Materials Today: Proceedings*, 46:5544-5549, 2021.

[42] Fadl, A. M., Abdou, M. I., Laila, D., and Sadeek, S. A. Fabrication and characterization of novel p-Phenylamine-N (4-chloro salicylaldenemine) ligand and its metal complexes and evaluation their anti-corrosion and chemical resistance properties in epoxy/SiO_2 nanocomposite for steel surface coating. *Chemical Engineering Journal*, 384:123390-123490, 2020.

[43] Kaniuk, Ł. and Stachewicz, U. Development and advantages of biodegradable PHA polymers based on electrospun PHBV fibers for tissue engineering and other biomedical applications. *ACS Biomaterials Science & Engineering*, 7(12):5339-5362, 2021.